



HAL
open science

Diffuse shear wave spectroscopy for soft tissue viscoelastic characterization

S. Beuve, L. Kritly, S. Calle, Jean-Pierre Remenieras

► **To cite this version:**

S. Beuve, L. Kritly, S. Calle, Jean-Pierre Remenieras. Diffuse shear wave spectroscopy for soft tissue viscoelastic characterization. *Ultrasonics*, 2021, 110, pp.106239. 10.1016/j.ultras.2020.106239 . hal-02949572

HAL Id: hal-02949572

<https://hal.science/hal-02949572>

Submitted on 21 Sep 2022

HAL is a multi-disciplinary open access archive for the deposit and dissemination of scientific research documents, whether they are published or not. The documents may come from teaching and research institutions in France or abroad, or from public or private research centers.

L'archive ouverte pluridisciplinaire **HAL**, est destinée au dépôt et à la diffusion de documents scientifiques de niveau recherche, publiés ou non, émanant des établissements d'enseignement et de recherche français ou étrangers, des laboratoires publics ou privés.



Distributed under a Creative Commons Attribution - NonCommercial 4.0 International License

Diffuse shear wave spectroscopy for soft tissue viscoelastic characterization

S. Beuve¹, L. Kritly¹, S. Callé², J-P. Remenieras¹

UMR 1253, iBrain, Université de Tours, Inserm, Tours, France.

GREMAN UMR 7347, Université de Tours, CNRS, INSA Centre Val de Loire, Tours, France

Abstract—In order to limit and slow the development of diseases, they have to be diagnosed early as possible to treat patients in a better and more rapid manner. In this paper, we focus on a noninvasive and quick method based on diffuse fields in elastography to detect diseases that affect the stiffness of organs. To validate our method, a phantom experiment numerically pre-validated is designed. It consists of seven vibrators that generate white noises in a bandwidth of [80-300] Hz and then a complex acoustic field in a phantom. Waves are tracked by a linear ultrasound probe L11-4v linked to a Verasonics Vantage System and are converted into a particle velocity 2D map as a function of time. The phase velocity of the shear waves is calculated using a temporal and 2D spatial Fourier transform and an adapted signal-processing method. Shear wave velocity dispersion measurement in the frequency bandwidth of the vibrators enables one to characterize the dynamic hardness of the material through the viscoelastic parameters μ and η in an acquisition time shorter than a second ($T_{acq}=300$ ms). With the aim of estimating the consistency of the method, the experiment is performed $N=10$ times. The measured elastic modulus and viscous parameter that quantify the dynamic properties of the medium correspond to the expected values: $\mu = 1.23 \pm 0.05$ kPa and $\eta = 0.51 \pm 0.09$ Pa·s.

Index Terms — complex acoustic field, elastography, rheology, ultrasound imaging

I. INTRODUCTION

The aim of the method presented below is to detect diseases that affect the stiffness of biological tissues to improve the care of patients and monitor their pathologies. Various studies show that there is a direct link between the viscoelastic parameters of the affected organs and diseases such as Alzheimer disease [1], tumors in the brain tissue [2], skin problems [3], or liver fibrosis [4]. Ultrasound elastography is a modality that quantitatively measures the elasticity of a material. In the medical field, it tends to complement or even substitute for palpation, which suffers from limitations such as its qualitative nature and the fact that it is a surface-based and operator-dependent examination method. The goal is to detect diseases as soon as possible and classify them by stage to slow their spread.

Vibration-Controlled Transient Elastography (VCTE) based on Fibroscan (Echosens, Paris, France) is considered today as the reference device to noninvasively assess liver stiffness, which has been shown to be a good surrogate marker of liver fibrosis [5]. One major issue when using VCTE is the necessity to find an optimal measurement window before triggering measurements. Indeed, the presence of artifacts like lungs, ribs or blood vessels disturbs the shear wave propagation and makes the stiffness estimation difficult

[6]. In this context, it would be interesting to develop a method that would make possible to analyze shear wave propagation even in the case of a complex and perturbed field. In radiation force elastography based method like Shear Wave Elasticity Imaging (SWEI) [7] or Shear Wave Elastography (SWE) [8,9] the shear wave is perfectly controlled with an ultrasound focused beam. The shear wave speed (SWS) is measured in the direction of the wave propagation to avoid the bias due to the presence of an angle between the direction of propagation and the direction of analysis. The main interest of our method is the fact that the shear sources position and their temporal evolution can be unknown. The presence of reflective structures, such as hard membranes around an organ, creates rebounds that expend the k-space of the acoustic field and reinforce the performance of our analysis with our approach.

Vibration sources can be passive: the physiological noise naturally present in the human body [10], pulsatility of the blood circulation, cardiac beating or muscle activities are all acting as shear wave sources. However, sources can be active by using external vibrators [5], loudspeakers [11,12] or using anatomical pathways as waveguide [5,13] without knowing exactly the position of the shear source. The central point of the algorithm is the time and 2D space Fourier transform to split the complex acoustic field into spatiotemporal frequencies assuming the medium locally isotropic and homogeneous. For each temporal pulsation ω , a 2D k-space analysis allows us to estimate the wave vector k of multiple waves that propagate in a soft medium. The phase velocity $c_s(\omega)$ is linked to the wave vector $k(\omega)$ and the pulsation ω by expression Eq.1:

$$c_s^2 = \omega/k(\omega) \quad (1)$$

By varying the pulsation ω , and carrying out the spatial analysis, we are able to measure the phase velocity evolution with frequency $c_s(\omega)$. Shear viscosity η is an important parameter to consider for the study of soft tissues [14]. Through a rheological model, the Voigt model in this study, shear elasticity μ and shear viscosity η are estimated from $c_s(\omega)$ dispersion. Since the medium is not purely elastic, we don't have the possibility to use the simple relation Eq.2:

$$\rho c_s^2 = \mu \quad (2)$$

where ρ is the medium density. This work is inspired by the time-reversal analysis of acoustic fields recently developed by S. Catheline [15] and the study led by H. Zhao [16], who designed directional filters that separate elementary shear waves which compose a complex diffuse field, e.g., they turned off all sources except the one in the selected direction.

The study is divided into two parts: a first part with simple case of a continuous progressive monochromatic plane wave source (Part II.A) and a second part with a more complicated field (Part II.B). Then, to

verify the reliability of our method, the phantom validation results are presented.

II. METHOD OF PHASE VELOCITY MEASUREMENT USING SPACE AND TIME FOURIER TRANSFORM

We are interested in the particle velocity field v induced by wave's propagation through a medium. Those waves are generated by sources randomly positioned in the imaging plane and with unknown temporal evolution. Since the field is composed of multiple waves which propagate in different directions pointed by their own wave number k , it is judicious for our analysis to use plane wave decomposition where we associate the plane wave magnitude A to the phase term in the classical form (Eq 3). To simplify the calculation, the complex plane wave expansion method is used for this study [17]. For each angular frequency ω , there is infinity of wave numbers going in all directions given by wave vector k (Eq 4). Thus, the complex particle velocity v and dispersion relation are:

$$v(\mathbf{r}, t) = \int_{0+}^{+\infty} \int_{-\infty}^{+\infty} \vec{A}(\vec{k}, \omega) \exp[j(\vec{k} \cdot \vec{r} - \omega t)] d\vec{k} d\omega \quad (3)$$

with:

$$k(\omega) = \omega / c_s(\omega) \quad (4)$$

The plane wave magnitude A at pulsation ω has significant magnitude if the wave vector k satisfies the dispersion relation (Eq 4).

A. Extract velocity from a monochromatic plane progressive wave

To explain the basics of the method, we use the simple case of a monochromatic plane wave (Eq 5) passing through a plane as follows:

$$v(z, x, t) = A \exp[j(k_{z0}z + k_{x0}x - \omega t + \varphi)] \quad (5)$$

$$\text{where: } c_s = \omega / \sqrt{k_{z0}^2 + k_{x0}^2}$$

The previous form of the signal can be rewritten as a function of the angle θ between the direction of propagation and the Oz axis (Eq 6).

$$k_{z0} = 2\pi \cdot \cos(\theta) / \lambda \text{ and } k_{x0} = 2\pi \cdot \sin(\theta) / \lambda \quad (6)$$

Now, we fix the time at instant $t = t_0$ and take a snapshot of a region of interest presented in the Figure 1.

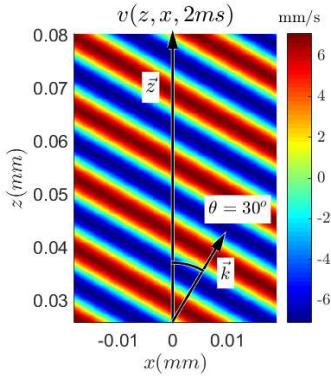


Fig. 1. Particle velocity $v(z, x, t = 2 \text{ ms})$ that propagates with angle $\theta = 30^\circ$.

The product of the time and frequency is associated with a constant phase shift $\varphi_1 = 2\pi f t_0 + \varphi = 0$:

$$v(z, x) = A \exp[jk_0(\cos \theta \times z + \sin \theta \times x)] \quad (7)$$

$$k_0 = \sqrt{k_{z0}^2 + k_{x0}^2} = 1/\lambda = \omega / c_s(\omega) \quad (8)$$

The particle velocity signal now being established, parameters of the wave field are chosen. As an example, the time frequency is $f = 100 \text{ Hz}$, the incident ray has an angle $\theta = 30^\circ$ from the axial axis z and the shear wave speed is imposed at $c_s = 1.15 \text{ m/s}$.

Then the space Fourier transform is used to measure the wave number. Both parameters ω and λ enable the calculation of velocity c_s as previously defined in equation (Eq 8).

The 2D space Fourier transform is applied to the particle velocity data at $v(f = 100 \text{ Hz}, \theta = 30^\circ)$ to find the wavelength λ and phase velocity c_s [18], which enables the calculation of the mean shear modulus μ of the medium in the region of interest if the density of the probe medium ρ is known. The complex signal $v(k_z, k_x)$ at $f = 100 \text{ Hz}$ contains information about the amplitude and direction of the wave because of the phase (Eq 9).

$$|v(k_z, k_x)| = A \delta(k_z - k_{z0}, k_x - k_{x0}) \quad (9)$$

For a monochromatic wave, since $k_0 = 2\pi f / c_s$ then $A_z \neq 0$ for only one point of coordinates (k_{x0}, k_{z0}) as presented in Figure 2.

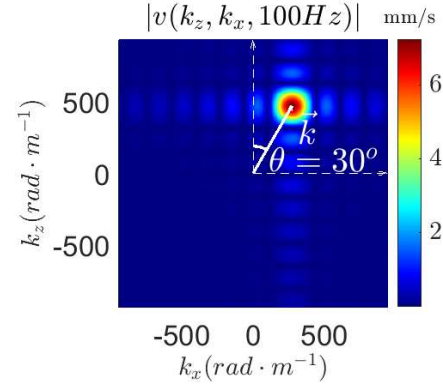


Fig. 2. Space Fourier Spectrum magnitude $|v_z(k_z, k_x)|$ from a plane shear wave $v_z(z, x, f = 100 \text{ Hz})$.

We can determine the direction of propagation of the waves and the source direction by finding the maximum of the magnitude $|v(k_z, k_x)|$ using method explained in section B. We find:

$$k_{z0} = 473 \text{ rad} \cdot \text{m}^{-1}, k_{x0} = 273 \text{ rad} \cdot \text{m}^{-1}$$

resulting in:

$$k_0 = \sqrt{(473 \text{ rad} \cdot \text{m}^{-1})^2 + (273 \text{ rad} \cdot \text{m}^{-1})^2} = 546 \text{ rad} \cdot \text{m}^{-1}$$

In this step, each parameter of the equation of the particle velocity is fully known (Eq 10), and it can be rewritten as a function of space and time with their values:

$$v(z, x, t) = A \exp[j((473 \text{ rad} \cdot \text{m}^{-1}) \times z + (273 \text{ rad} \cdot \text{m}^{-1}) \times x - 2\pi(100 \text{ Hz}) \times t)] \quad (10)$$

Finally, with frequency f_0 , velocity $c_s(f_0)$ can be deduced by finding the location of A as a non-zero value and applying equation 13. With the spatiotemporal frequencies ($k_0 = 546 \text{ rad} \cdot \text{m}^{-1}$, $f_0 = 100 \text{ Hz}$), the phase velocity is approximately $c_s(100 \text{ Hz}) = 1.15 \text{ m/s}$. The value calculated is equal to the imposed one.

B. Extract velocity from a complex wave field

Now, let us take the example of a complex acoustic field that came from multiple sources at same frequency. In this case, assuming isotropy of sources, waves originate from all around the region of interest. Assuming linear acoustic, waves propagate independently in different directions and create an interference pattern which continuously changes with time. This situation is equivalent to the sum of multiple monochromatic plane waves, as represented in Figure 3. Our method enables us to determine the direction of acoustic sources all around the region of interest.

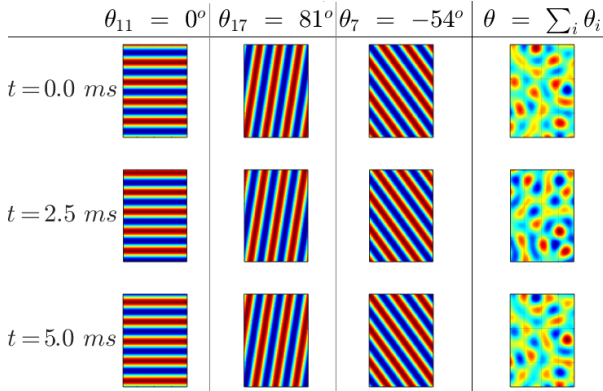


Fig. 3. Real part of the particle velocity for a diffuse field (21 acoustic sources) at 3 instants.

That complex field, shown in Figure 3, was computed with $N_s = 21$ acoustic sources excited at frequency $f = 100$ Hz, which were distributed all around a material from $\theta = -135^\circ$ to 135° with an angle between sources of $\Delta\theta = 13.5^\circ$. The empty space, between sources 1 and 21 in Figure 4, represents the location of a probe and anticipates the experimental part of this study. The grid for this mathematical model contains vectors of length $N_z = 362$, $N_x = 248$ with identical spatial resolutions $\Delta z = \Delta x = 150 \mu\text{m}$.

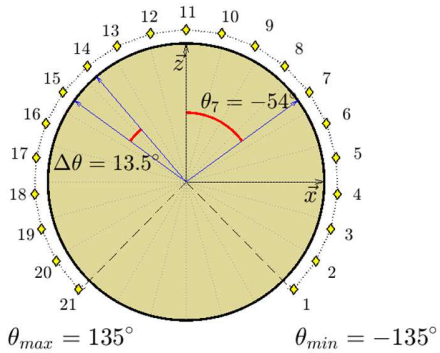


Fig. 4. Drawing of 21 sources setup around a circular medium from -135° to 135° with 13.5° between sources.

As previously, the space Fourier transform is applied to the data. To improve the space resolution, zero padding is used. The performance of the fast Fourier transform algorithm is optimized when the lengths of the transformed signal are an exact power of two in each dimension; thus, we take the power of two superior to the length of the vector and fill the void with zeros [19]. To obtain an identical frequency resolution on between z and x axes, lengths must be identical for both directions x and z because the original spatial resolutions are equal $\Delta z = \Delta x$. Sampling parameters are grouped in Table 1 (part III.).

For a homogeneous and isotropic medium, the velocity remains identical everywhere and is independent of the propagation's direction. If the resolution in each direction is the same, then the spectrum $|v(k_z, k_x)|$ of the diffuse field is a ring around the center $(k_z, k_x) = (0; 0)$. This spectrum is a Dirac delta function summation that forms a circle drawn on Figure 4.

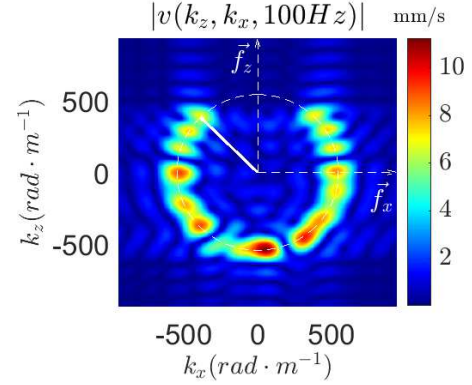


Fig. 5. Space Fourier Spectrum magnitude $|v_z(k_z, k_x)|$ of the diffuse field constructed from 21 plane shear waves.

Obviously, there is no source at the location of the ultrasonic sensor, so the ring will not be complete as shown in Figure 5. As presented in Figure 4, no wave comes from the probe to the medium in the z axis direction, which explains the blank space in its front. We can approximately measure the radius by selecting the maximum of a high amplitude peak. For example, the maximum is located near $k_x = 0 \text{ rad}\cdot\text{m}^{-1}$ and $k_z = -500 \text{ rad}\cdot\text{m}^{-1}$. Unfortunately, this is no optimal method because it does not take account the 2D characteristics of the spectral data.

Some problems prevent us from properly determining the velocity of shear waves, such as the finite length of the signals, the sampling, the medium attenuation or the multiplicity of the sources. Those problems induce issues such as the lack of resolution, periodization of the spectrum and interferences, which constrain us to use techniques to find the closest value of the mean phase velocity of the shear waves. To remove the side lobe effect and inconstancy of the spectrum, we imagine what appears similar to the spectrum of a perfect theoretical diffuse field $|v_T(k, c)|$, which represents a circular continuous array of isotropic sources placed all around a medium [20]. In the 2D space Fourier domain, $|v_T(k, c)|$ is ideally a circle of Dirac functions $1/\lambda$ away from the origin. Following this reasoning the template of reference spectrum can be modeled in 2D by a Gaussian function (Eq 11) with both mean value and standard deviation variable and a high order n .

$$|v_T(k, c)| = \exp\left[-\frac{1}{2}\left(\frac{k-k_0}{\sigma_g}\right)^{2n}\right], \begin{cases} k_0 = \omega/c \\ \sigma_g = \frac{W/2}{(2\log 2)^{1/2n}} \end{cases} \quad (11)$$

σ_g is the standard deviation of the Gaussian that is linked to the spectrum obtained from the data, n is the order of the Gaussian function, and W is the full width at half maximum (FWHM) of the peak. A higher order of the Gaussian corresponds to a steeper slope of the curve and a tray in the summit. To have a good compromise between the gate and the Gaussian functions, we increase the order n to three as drawn in Figure 6.

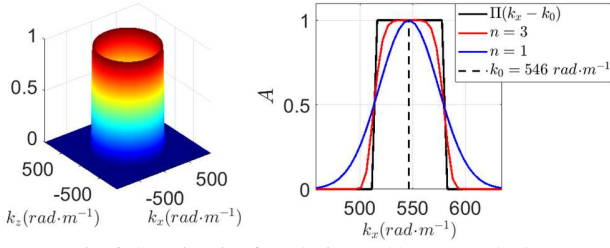


Fig. 6. Gaussian ring for velocity $c_s(100 \text{ Hz}) = 1.15 \text{ m/s}$; standard deviation $\sigma_g = 1.88 \text{ rad}\cdot\text{m}^{-1}$; order $n = 3$.

Gaussian crowns $|v_T(c)|$ are generated for several velocity values $c = [0.8:0.01:1.8] \text{ m/s}$, multiplied with the result of the space Fourier transform of the particle velocity data $|v|$ to create the function $\gamma(c)$ (Eq. 12):

$$\gamma(c) = |v| \times |v_T(c)| \quad (12)$$

The summation of $\gamma(c)$ over all points in the 2D space gives the autocorrelation value at lag 0 (Eq. 13).

$$\Gamma(c) = \sum_{k_z} \sum_{k_x} \gamma(c) = \sum_{f_z} \sum_{f_x} |v| \times |v_T(c)| \quad (13)$$

These values $\Gamma(c)$ give information about similarity between the template $|v_T(c)|$ and the complex acoustic field $|v|$ created by 21 sources.

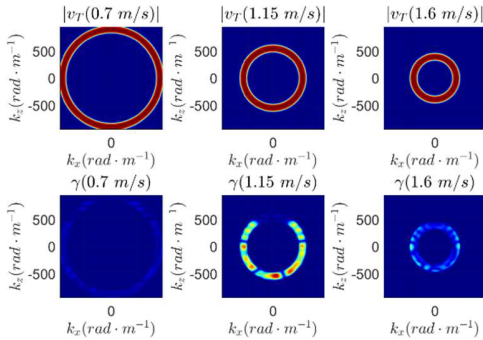


Fig. 7. Upper line: Gaussian crown for several velocity values $c = [0.7;1.15;1.6] \text{ m/s}$. Lower line: $\gamma(c)$ corresponding to the multiplication of $|v_T(c)|$. The resulting correlation $\Gamma(c)$ are respectively $\Gamma(0.7 \text{ m/s}) = 1.1 \text{ m}^2/\text{s}^2$, $\Gamma(1.15 \text{ m/s}) = 9.2 \text{ m}^2/\text{s}^2$, $\Gamma(1.6 \text{ m/s}) = 2.4 \text{ m}^2/\text{s}^2$.

The Gaussian crowns are plotted on Figure 7 for $c = 0.7 \text{ m/s}$, $c = 1.15 \text{ m/s}$ and $c = 1.6 \text{ m/s}$. The corresponding $\gamma(c)$ function for these three values c is then computed and the results presented in Figure 7. The corresponding Γ values are $\Gamma(0.7 \text{ m/s}) = 1.1 \text{ m}^2/\text{s}^2$, $\Gamma(1.15 \text{ m/s}) = 9.2 \text{ m}^2/\text{s}^2$ and $\Gamma(1.6 \text{ m/s}) = 2.4 \text{ m}^2/\text{s}^2$. The maximum of the Γ function provides us the mean wave velocity c . A bell curve is observed in Figure 8, so a parabolic interpolation around the three highest values enables us to omit the sampling effects.

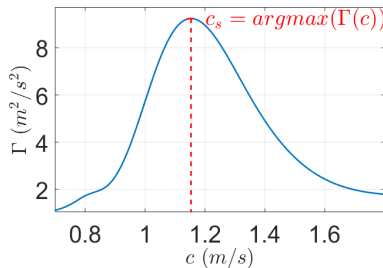


Fig. 8. The coefficient correlation $\Gamma(c)$ corresponding to the multiplication of $|v|$ by $|v_T(k,c)|$ with $c = [0.8:0.01:1.8] \text{ m/s}$ in function of the celerity c .

$$c_s = \arg \max(\Gamma(c)) \quad (14)$$

The value given by the algorithm is the mean velocity of the waves in the entire region of interest is $c_s = 1.145 \text{ m/s}$ (Eq 14). This result coincides with the imposed value of the shear wave velocity with an error $\varepsilon = 0.43 \%$.

III. PHANTOM VALIDATION

The method will be applied to experimental data using identical parameters. First, it will be applied to plane waves that propagate in two different directions. Second, it will be applied to a diffuse acoustic field. To generate shear waves, electro dynamic exciters (EX 45 S-8 Ω from VISATRON®, Germany) are used. The waves cross phantoms of different shapes depending on the requirements of the experimental setup: parallelepiped for the plane waves and cylindrical for the diffuse field. The shapes are homemade soft gels made of triblock SEBS copolymer (Kraton Polymers, Univar, France) dissolved in white mineral oil. The scatters used were silica powder [21]. The speed of ultrasound in those media is fixed to $c_p = 1450 \text{ m/s}$.

For phantom experiments, data are recorded by a Verasonics® ultrasound scanner (Kirkland, WA 98034, USA) with the Vantage platform in the ultrafast mode (>1000 frames per second) and plane wave imaging. A 128-elements linear array transducer L11-4v working at $f_{us} = 6.5 \text{ MHz}$ is used. A classical Delay And Sum (DAS) beamforming with $F\# = 1$ is applied on experimental data. Each frame is made from the sum of $n_a = 3$ planes with angles of $\alpha = [-3^\circ, 0^\circ, 3^\circ]$, an interval of $\Delta t_{nxa} = 150 \mu\text{s}$ between planes and a pause of $\Delta t_{nxf} = 200 \mu\text{s}$ for the next frame (Fig. 9). The image framerate is $\text{PRF} = 2 \text{ kHz}$, which corresponds to an interval of $\Delta t_{prf} = 500 \mu\text{s}$ between frames (Eq 15).

$$\Delta t_{\text{PRF}} = (n_a - 1) \times \Delta t_{\text{nxa}} + \Delta t_{\text{nxf}} \quad (15)$$

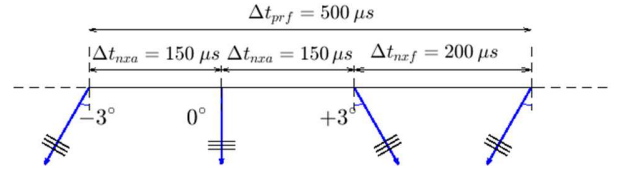


Fig. 9. Ultrasound imaging sequence with 3 angles

The lateral resolution is $\Delta x = 150 \mu\text{m}$ with a transducer pitch of $300 \mu\text{m}$. Data are sampled at $4 \times f_{us}$ but beamformed at a fraction of the probe pitch for the axial resolution (Eq 16).

$$\Delta x = \text{pitch}/2, \Delta z = \text{pitch}/10 \geq c_p/8f_{us} \quad (16)$$

This setting is done to easily obtain an identical spatial resolution in the 2D spatial Fourier domain and no longer dependent on the speed of ultrasonic wave c_p . The acquisition duration is simply determined from all delays and the number of frames $N_t = 700$ frames (Eq 17).

$$T_{\text{acq}} = N_t \times \Delta t_{\text{PRF}} = 700 \times 500 \mu\text{s} = 350 \text{ ms} \quad (17)$$

The US scanner gives access to raw data, which are transferred to the computer for post-processing. The delay-and-sum beamforming method is used to convert the data into radio frequency (RF) data [22]. The RF data are converted to complex IQ data (In-phase data, Quadrature data) with a numerical Hilbert transform along the O_z axis. Then, the temporal lag 1 autocorrelation is applied to the images to calculate the axial particle velocity v_z and edit a movie in the

imaging plane, where we observe propagating waves (Eq 18).

$$v_z\left(z - \frac{\text{lap}_z}{2}, x - \frac{\text{lap}_x}{2}, t - \frac{\text{lap}_t}{2}\right) = -\frac{\lambda}{4\pi\Delta t_{\text{PRF}}}\Delta\Phi \quad (18)$$

where:

$$\Delta\Phi = \arg\left[\sum_{a=0}^{\text{lap}_z-1}\sum_{b=0}^{\text{lap}_x-1}\sum_{c=0}^{\text{lap}_t-1}IQ(z-a, x-b, t-c)IQ^*(z-a, x-b, t-c-1)\right]$$

As previously mentioned, the particle velocity is a function of the phase, so the ambient noise strongly disrupts the measurement regardless of the signal-to-noise ratio. To avoid parasitic phase shifts, especially when the Doppler signal is weak, the correlation is made on a small spatiotemporal volume, which is moved on the matrix, as explained in Figure 10 [23]. This process naturally degrades the resolution but is necessary to smooth the signal. The spatial window $\text{lap}_z = 40 = 5\text{lap}_x$ is selected, which is five times higher than $\text{lap}_x = 8$. Then the size of the 3D block of data considered for the phase estimation is $1.2 \text{ mm} \times 1.2 \text{ mm} \times 3 \text{ ms}$ (Fig. 10). Windows and shifts values are not randomly chosen. We want axial and lateral resolutions at same size for particle velocity map then the 2D space block is shifted by five points axially (5 over 40, i.e. 12.5 % shift) and one point laterally (1 over 8, i.e. 12.5 %).

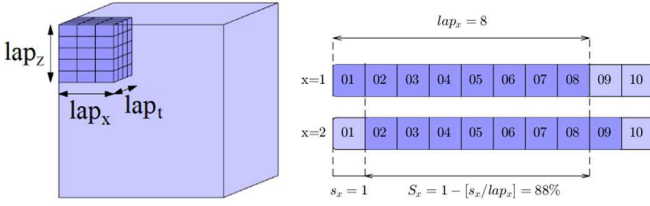


Fig. 10. Correlation with a 3D kernel of length lap_z , lap_x , lap_t .

The axial and lateral overlaps $S_z = S_x = 88\%$ are identical and we have the same spatial resolution as the simulation with $\Delta z = \Delta x = 150 \mu\text{m}$.

This particle velocity movie is used to measure the wave speed with space and time Fourier transform. Then, the elasticity is deduced using equation 1. The resolution setting and number of points for these experiments are identical to the presented simulations for comparison. All sampling parameters are listed in the table 1 below:

TABLE I
RESOLUTION OF THE PARTICLE VELOCITY DATA MATRIX

	Axial component z	Lateral component x	Time component t
RF size	$N_z = 1846$	$N_x = 255$	$N_t = 700$
RF resolution	$dz = 30 \mu\text{m}$	$dx = 150 \mu\text{m}$	$dt = 500 \mu\text{s}$
Lap	$\text{Lap}_z = 40$	$\text{Lap}_x = 8$	$\text{Lap}_t = 6$
Shift	$s_z = 5$	$s_x = 1$	$s_t = 1$
Overlap	$S_z = 88\%$	$S_x = 88\%$	$S_t = 83\%$
V size	$N_z' = 362$	$N_x' = 248$	$N_t' = 694$
V resolution	$\Delta z = 150 \mu\text{m}$	$\Delta x = 150 \mu\text{m}$	$\Delta z = 500 \mu\text{s}$

A. Experimental validation for plane wave

The experimental setup is shown in Figure 11. A 100 Hz continuous sinusoidal wave generator supplies a shaker, which is linked to the plate, to create a plane wave into a parallelepiped phantom, whose dimensions are $115 \text{ mm} \times 60 \text{ mm} \times 50 \text{ mm}$ and where shear waves propagate at speed $c_s = 1.63 \text{ m/s}$.

Two measurements are made: first, a plate is placed on the side of the probe; second, the plate is facing the probe. This device verifies whether the Fourier transform method works in the simple case of

monochromatic plane waves.

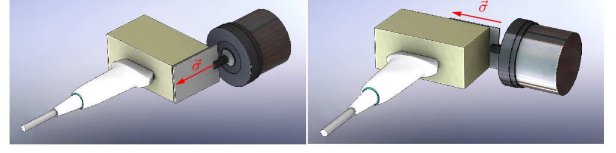


Fig. 11. Left: exciter on the side of the US probe generating a plane $v_z(z,x,t)$ shear wave. Right: exciter in front of the US probe generating a plane $v_x(z,x,t)$ shear wave.

With a plane condition, the shear wave is purely transversally polarized, and the displacement of the medium particles is collinear to the z-axis when the plate is on the side of the phantom and the wave propagates along x. The Dirac delta function is located on the k_x -axis at approximately $-500 \text{ rad}\cdot\text{m}^{-1}$.

Hence, conventional elastography imaging techniques are used (Eq 18) to compute the axial particle velocity: $v = v_z(z,x,t)$ (Figure 12).

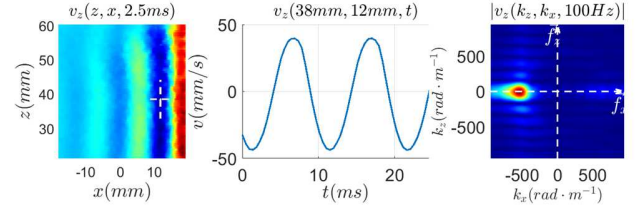


Fig. 12. Left: axial particle velocity $v_z(z,x,t = 2.5 \text{ ms})$. Center: temporal evolution of the particle velocity $v_z(38 \text{ mm}, 12 \text{ mm}, t)$ (at point A). Right: 2D velocity spectrum $v_z(k_z, k_x, f = 100 \text{ Hz})$.

As expected, a Dirac function is located on the k_x -axis at approximately $-500 \text{ rad}\cdot\text{m}^{-1}$ in the k -space (Fig. 12). Thus, our method works if the waves can be observed in the particle velocity movie at each sampling time t_i . When the plate is placed in front of the probe, the waves propagate along the z axis, but the particle movements are purely lateral, so the particle velocity along the z-axis is zero. This lateral component of the particle velocity $v = v_x(z,x,t)$ is computed using vector velocity imaging method already proposed by our group for *in vivo* contractile properties measurement of muscle [24].

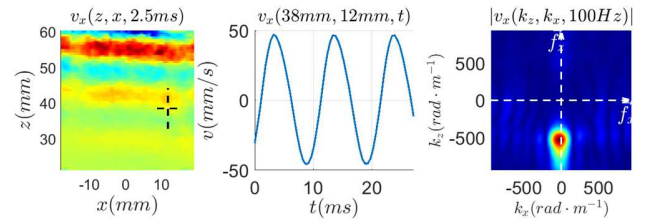


Fig. 13. Left: axial particle velocity $v_x(z,x,t = 2.5 \text{ ms})$. Center: temporal evolution of the particle velocity $v_x(38 \text{ mm}, 12 \text{ mm}, t)$ (at point A). Right: 2D velocity spectrum $v_x(k_z, k_x, f = 100 \text{ Hz})$.

The wave arrives from the top and propagates in the direction of the bottom image, as seen in Figure 13, meaning the wave vector is oriented to the bottom. The Dirac delta function is located on the k_z -axis at approximately $-500 \text{ rad}\cdot\text{m}^{-1}$. The corresponding wavelength λ is the same than for the first configuration using the axial particle velocity $v_z(z,x,t)$. For accuracy, the crown cross-correlation is applied to the experimental data to find a precise velocity value. The obtained velocity in each direction is $c_{sz} = 1.59 \text{ m/s}$ and $c_{sx} = 1.57 \text{ m/s}$ each at

100 Hz. Both results are quite similar even if the slight difference due to signal noise ratio than are different for estimated axial and lateral velocities.

B. Experimental validation for complex wave field

The experimental setup is shown on Figure 14. Seven electro dynamic exciters are set around a soft phantom, whose characteristics are as follows: diameter $d = 120$ mm, density $\rho = 905$ kg/m³ where shear waves propagate at approximately $c = 1.1$ m/s. The vibrators are held by homemade 3D-printed adjustable holders to perfectly fit the shape of the medium. The 3D-printed L-shaped stems with square toes $S = 10$ mm \times 10 mm are stuck on the flat surface of the vibrators to generate preferentially shear waves into the region of interest. Because of the relatively reduced dimensions of the phantom, if we consider the size of human organs and wave attenuation in the medium, only seven sources can be placed. Those electro dynamic exciters are each driven by amplifiers (Velleman modules Stereo Amplifier Module 2×30 W VM113) with seven different noise generators from identical bandwidth $B_v = [80-300$ Hz]. We generate those noises to get closer to the passive elastography measurement conditions [25], which enables us to calculate the dispersion of the phantom elasticity E in the bandwidth.

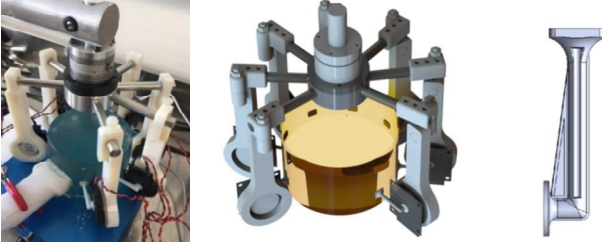


Fig. 14. Left: Photograph of the experimental system. Center: drawing of the experimental system setup. Right: L-shape stem with square toe fixed of the plate of vibrators in order to generate a shear wave source condition.

To justify this source arrangement, we examine the case of a vibrator, whose stem is tangent to the gel at an angle of $\theta = -90^\circ$ and vibrates in the z direction ($\theta = 0^\circ$). The geometry is defined in Figure 16 with σ vertical and upwards. Radiation patterns show that it is necessary to exert tangential movements to the gel surface to generate shear waves [26]. Furthermore, stems whose toes are the size of the wavelength of the shear wave $\lambda_s \sim 1$ cm at 150 Hz induce a strongly diffracted shear wave. Finally, by adding the contributions on the x and z -axes, the displacement of a point source that emits a temporal Dirac signal is determined. The other radiations of other vibrators are obtained by simply rotating the radiation patterns g_{xz} and g_{zz} around the phantom. The change of basis from is made by rotation using matrix $R(\theta_j)$ (Eq 19):

$$R(\theta_j) = \begin{pmatrix} \sin(\theta_j) & -\cos(\theta_j) \\ \cos(\theta_j) & \sin(\theta_j) \end{pmatrix} \quad (19)$$

The phantom is assumed to be a linear time-invariant (LTI) system to calculate the response to any mechanical stress by simply convoluting it with the impulse response, *i.e.*, the Green functions (Eq 20).

$$\vec{u} = [g_{13} \sin(\theta_j) - g_{33} \cos(\theta_j)] \vec{e}_x + [g_{13} \cos(\theta_j) + g_{33} \sin(\theta_j)] \vec{e}_z \quad (20)$$

And then taking advantage of the convolution derivations properties we can deduce the shape of the particle velocity impulse response by derivating the stress function σ_j (Eq 21).

$$\mathbf{v}_{zj}^s(\mathbf{r}, t) = \mathbf{g}_{zj}^s(\mathbf{r}, t) \otimes \partial_t \sigma_j(t) \quad (21)$$

This relation shows that displacement and velocity have identical radiation patterns; the only difference is the temporal shape of the wave. With knowledge about the Green functions, we can determine the shape of the waves that radiate in the probed soft material (Figure 15). L-shaped stems are used to polarize shear waves in the axis of these stems to make them converge at the center of the gel, where is the region of interest.

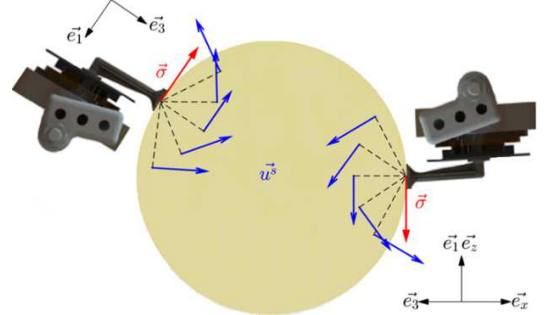


Fig. 15. Displacement vector u induced by two vibrators with a shear stress applied to the surface of the phantom. The reference frame e_x, e_y, e_z is fixed and the other reference frames e_1, e_2, e_3 are linked to exciters around the phantom.

Another point to carry out is the fact that compression waves are notably fast: approximately $c_p \sim 1500$ m/s, which results in a significantly long wavelength of $\lambda_p \sim 10$ m at $f = 100$ Hz. The gel is distorted instantaneously in the whole region compared to the Doppler time base but with different amplitudes due to attenuation and diffraction.

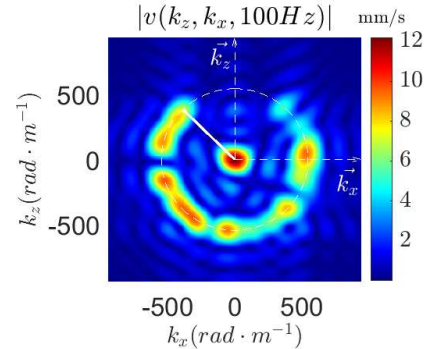


Fig. 16. 2D space Fourier transform $|v(k_z, k_x, 100\text{Hz})|$ of the complex shear wave field $v(k_z, k_x, f = 100$ Hz) with an additional compression wave situated at the origin of the (k_z, k_x) grid.

Even if theoretically the amplitude of the P-wave is one million times smaller than S-wave $(c_p/c_s)^2 > 10^6$, P-waves are present in our experiment. Their associated space frequencies $1/\lambda_p$ tend toward zero and appear like a spot in the center of 2D spatial Fourier transform (Eq 22), as shown in Figure 16.

$$k_p = \frac{2\pi}{\lambda_p} = \frac{2\pi f}{c_p} = \frac{100 \text{ Hz}}{1540 \text{ m.s}^{-1}} = 0.4 \text{ rad} \cdot \text{m}^{-1} \quad (22)$$

IV. RESULTS AND DISCUSSION

We are interested in measuring dispersion of shear velocity as function of frequency. Thus, the time component of the Doppler axial particle velocity is Fourier transformed to indicate the frequencies of the propagating waves in the phantom.

$$v(z, x, t) = v_z(z, x, t)$$

As shown in Figure 17, a point A is selected in the ROI at $(z_a; x_a)$ near the border of the ROI, where waves are not much attenuated at

this location.

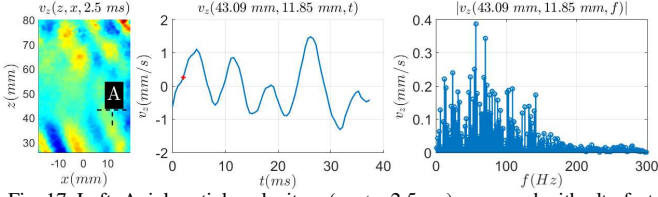


Fig. 17. Left: Axial particle velocity $v_z(z, x, t = 2.5 \text{ ms})$ measured with ultrafast US imaging. Center: temporal evolution of $v_z(43.09 \text{ mm}, 11.85 \text{ mm}, t)$ (at point A). Right: time Fourier transform of the measured particle velocity $|v_z(43.09 \text{ mm}, 11.85 \text{ mm}, t)|$ (at point A).

In Figure 17, the spectrum extends up to the peak near 150 Hz and small magnitudes are observed. The wave at a particular point is the summation of all the S-waves generated by the 7 vibrators. Since the temporal evolution of vibrations are not the same and the observation point can be random, the resulting wave is a summation of sometime constructive and at another time destructive that leads to a small magnitude. For this reason, the temporal evolution of the particle velocity and its spectrum shown in Figure 17 are highly variables. At low frequency, since there is a weak attenuation it results a high magnitude. When the frequency increases, the attenuation does as well, resulting in a magnitude loss. Now by fixing the time frequency, we can highlight the wavelength using the time Fourier transform. The complex acoustic field can be decomposed into monochromatic waves through the time Fourier transform simply by selecting a frequency and plotting it in the imaged region as shown in Figure 18.

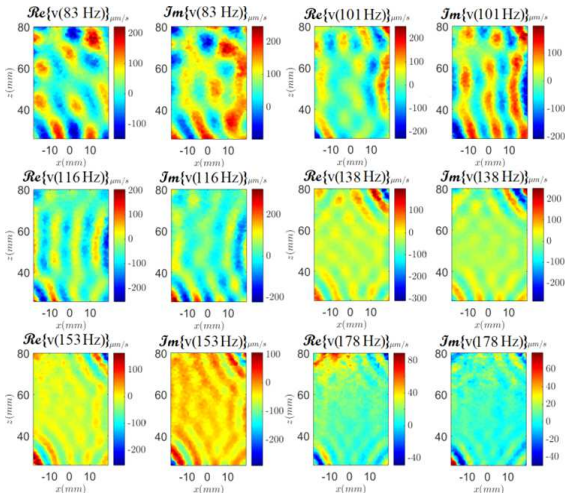


Fig. 18. Real and imaginary parts of the particle velocity $v_z(z, x, f)$ at several time frequencies $f = [83, 101, 116, 138, 153, 178] \text{ Hz}$.

With this representation, we can determine that the directions of the sources are behind the concave part of the waves. It is interesting to note that the 2D interference patterns of real and imaginary parts of $v_z(z, x)$ in Figure 18 are not exactly the same for the different selected frequencies in the temporal spectrum. For example, at 83 Hz the field is highly variable and this is difficult to predict the position of vibrators. However, at 101 Hz waves are more regular and rather vertical with a clear visualization of the wavelength. And at high frequency we can see the position of some sources.

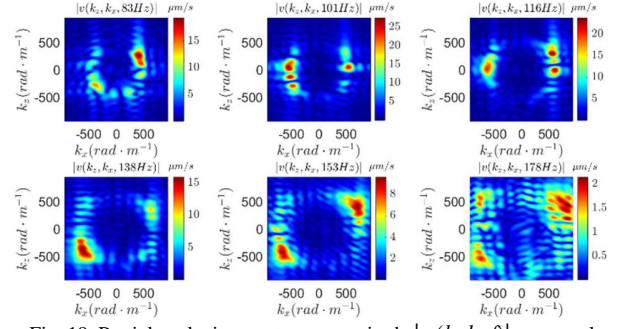


Fig. 19. Particle velocity spectrum magnitude $|v_z(k_z, k_x, f)|$ at several frequencies $f = [83, 101, 116, 138, 153, 178] \text{ Hz}$.

The following results of the time-space Fourier transform on experimental data are obtained and plotted for several time frequencies in the k -space in Figure 19. The circle radius $2\pi/\lambda$ increases with frequency. As shown visually on Figure 19, we notice the dominance of some sources at each frequency simply based on the magnitude of the spectrum. We also notice a widening of the spectrum of our particle velocity data $|v_z(k_z, k_x, f)|$ as a function of the frequency in our analysis bandwidth. The reason for this growth is due to the shear wave attenuation in the phantom involving a term convoluted with our imposed excitation. The Fourier transform of $\exp(-\alpha r)$ is the function $1/(\alpha + jk)$ which its magnitude is a bell-shaped curve. The FWHM is a function of α which increase with frequency since the attenuation α increase with frequency. We measure the full width at half maximum W of the spectrum of our data at several frequencies (Fig. 20). Then we perform a first order interpolation to adjust the calculation of Gaussian rings $|v_T(k, c)|$ (Eq. 11) with frequency. This broadening effect could be used to estimate the viscosity but the main part of the attenuation is due to wave diffraction which is an unknown of our problem.

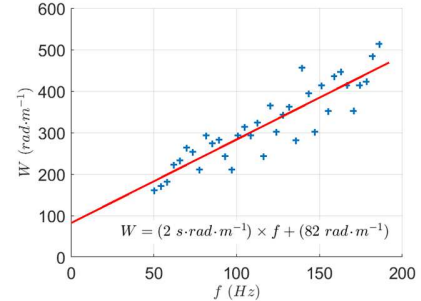


Fig. 20. Spectrum width W in a plane section of k as a function of the time frequency f .

Then, the cross-correlation algorithm is applied at each time frequency to determine the $\Gamma(f, c)$ functions. Similar to the simulation part, the maximum of each $\Gamma(c)$ function indicates the velocity $c_s(f)$ of the shear waves that pass through the medium for each frequency.

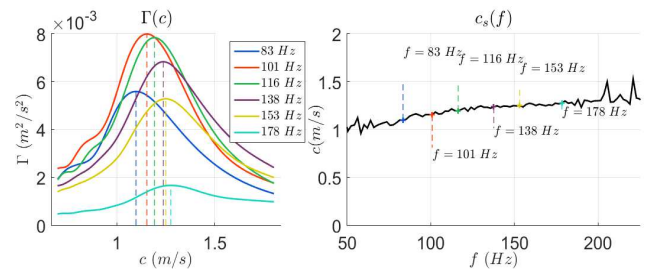


Fig. 21. Left: Γ function at six frequencies. Right: Shear wave velocity as a

function of the frequency

In Figure 21, we can notice that there is no ambiguity for the c determination from $I(c)$ for each frequency in the analysis bandwidth. Because of the measurement errors, sampling and particularity attenuation, the analysis is limited to 192 Hz. To illustrate this point, the maximum of the axial particle velocity amplitude A_z is plotted on Figure 22 as a function of frequency from 50 Hz to 270 Hz in order to highlight the attenuation effect.

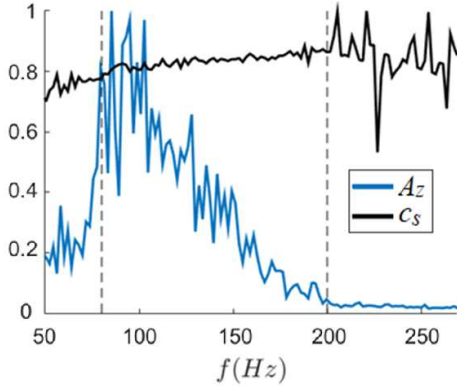


Fig. 22. Normalized axial particle velocity amplitude A_z as a function of the frequency compared to the normalized shear wave velocity dispersion curve c_s .

In our frequency selection, the signal decreases according to the frequency and after the upper band, it drops significantly. Furthermore, a sudden fall is observed before the low band. At one fixed frequency, in the case where the signal to noise ratio is too low, our correlation algorithm will not recognize the spectral ring and will return a false value. From the dispersion curve $c_s(f)$ shown in Figure 21, we deduce the medium shear viscoelastic parameters (μ, η) . Using a dynamic mechanical analysis, the phantom can be modeled by a purely elastic spring μ and a purely viscous damper η in parallel, as established by the Kelvin-Voigt material model. This dynamical model yields the relation between the strain ε of the probed medium and the applied stress σ to generate that strain (Eq 23). This model is described by a differential equation depending on viscoelastic parameters:

$$\sigma(t) = \mu\varepsilon(t) + \eta\dot{\varepsilon}(t) \quad (23)$$

Then, we can calculate the complex space frequency. Using the ratio of the complex time-space frequency (Eq 24), we can find the velocity of shear waves. Thus, the shear wave velocity depends on the viscoelastic parameters [27]:

$$c_s(\omega) = c_{s0} \sqrt{\frac{2\left(1 + \left(\frac{\omega\eta}{\mu}\right)^2\right)}{1 + \sqrt{1 + \left(\frac{\omega\eta}{\mu}\right)^2}}}, \text{ with } c_{s0} = \sqrt{\frac{\mu}{\rho}} \quad (24)$$

From the values of $c_s(\omega)$, using nonlinear least-squares minimization method from equation 24, the viscoelastic parameters (μ, η) are deduced from 80 to 196 Hz as shown in Figure 23. We obtained the values $\mu_1 = 1.17$ kPa and $\eta_1 = 0.62$ Pa·s.

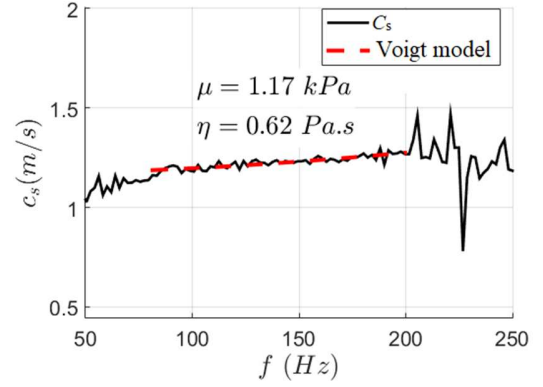


Fig. 23. Voigt model superposed to the measured shear wave velocity dispersion curve

To ensure that the experiment is repeatable, $N = 10$ measurements with identical configurations and with different white noise signals were performed and plotted in Figure 24. The values of viscoelastic parameters for each experiment and their medians and IQR were calculated and listed in Table 2.

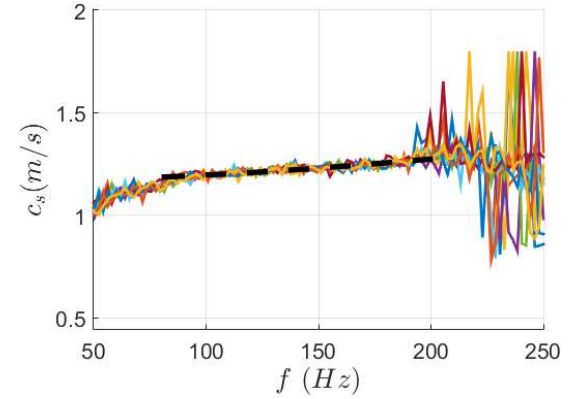


Fig. 24. Phase velocity as a function of frequency for $N = 10$ experiments

TABLE II
RESULTS OF THE VISCOELASTIC PARAMETERS MEASUREMENT

Experiment number N	Elastic Modulus μ (kPa)	Viscous modulus η (Pa·s)
01	1.17	0.62
02	1.25	0.4
03	1.20	0.58
04	1.25	0.46
05	1.23	0.52
06	1.25	0.48
07	1.19	0.60
08	1.23	0.51
09	1.24	0.50
10	1.22	0.54
Median	1.23	0.53
IQR	0.05	0.09

According to Equation 24, SWS dispersion is quantified by the parameter $\omega\eta/\mu$ which is the ratio between viscosity effect and elasticity effect. Thus, the slope of the dispersion curve is not a measurement of the viscosity but a measurement of the significance of one effect relative to the other. If the dispersion slope is the same for two different elasticities, this implies that the viscosity follows the same proportion of change. A purely linear solid without viscosity will give a constant curve with frequency. The elastic parameter μ estimated at 0 Hz will be in this case equal to the measured value obtained from the Voigt model and the viscosity will be insignificant.

In Figure 23, we measured a small variation of the SWS with frequency. As shown in Figure 24, with 10 acquisitions, these measurements are highly repeatable. The elastic modulus has an IQR of 0.05 kPa and the shear viscosity an IQR of 0.09 Pa·s.

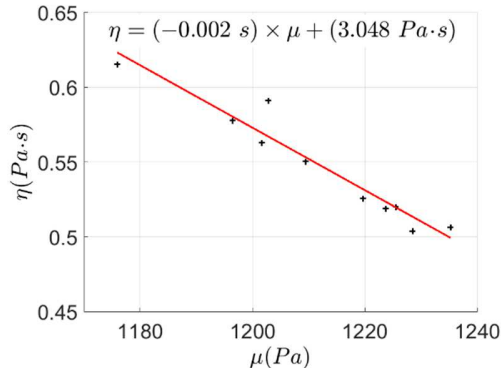


Fig. 25. Viscous parameter η versus elastic parameter μ for each measurement

We notice in Figure 25 that when the measured shear modulus μ is high, the associated viscosity is rather small. It is due to a change in the slope of $c_s(f)$ which is very sensitive to small variations induced by noise peaks at high frequency. A relatively low slope will give a high shear elasticity obtained at 0 Hz and a relatively small viscosity. Inversely, a relatively higher slope will give a shear elasticity at zero frequency smaller, associated with a higher viscosity. We observe that SWS curvature increase more rapidly when frequency decreases under 80 Hz for all 10 measurements. This reason pushed us to restrict the frequency band for the application of the Voigt rheological analysis above this frequency. The SWS is around 1.2 m/s at 80 Hz (Fig. 24), thus the shear wavelength is 1.5 cm. This wavelength is even much lower than the size of the phantom which is 12 cm diameter. Then boundary effects appear because of phantom dimension which are close to the wavelength. The same trend is obtained by Kijanaka [28] and also by Sack [29]. The fast variation of the SWS at very low frequency can be due to presence of guided wave [30] but we have volume wave and not guided wave in our experiment. One possible explanation is a near field effect due to diffraction. Our sources have a 1 cm² size which is smaller than the 1.5 cm wavelength. In this case the radiation is complex and the spatial derivation of the wave phase $\partial\Phi/\partial r$ is not linear with the position r and the plane wave approximation is not valid. $c_s(\omega)$ at a particular frequency is $c_s(\omega) = \omega/(\partial\Phi/\partial r)$ which is not equal to ω/k in the near field. From the ten acquisitions, we obtained $\mu = 1.23 \pm 0.05$ kPa for the shear elastic modulus and $\eta = 0.53 \pm 0.09$ Pa·s for the shear viscosity of our phantom.

V. CONCLUSION AND OUTLOOKS

The presented spectrum cross-correlation method enables us to calculate the dynamic viscoelasticity in the region of interest by measuring the mean velocity in this area. The reliability of the method increases with the increase in number of repetitions N of the experiment. The experiment is extremely fast (less than one second per acquisition). Furthermore, it works with complex acoustic fields to provide an active measurement. The position of the source is an unknown of the inverse problem and it is not a limitation for this method unlike main transient elastography methods. For future *in vivo* experiment, both active and passive measurements are available, and the waves can be created by physiological noise. Nevertheless, the algorithm is memory-consuming: more than 10 Million elements with double-precision 64 bites per element). Some parameters must

be manually adjusted, such as the shape of the mask, which require us to consider the medium homogeneity.

When plan to use our method *in vivo* to estimate the liver rheology using vibrators situated all around the volunteer rib cage. This offers an elegant solution to solve the complicated problem of the wave field disturbance due to the presence of the ribs in TE. We will also use our method for thyroid elastography using complex physiological field created by our voice. The preliminary results obtained singing a linear chirp in the 100-300 Hz bandwidth was very promising. We can visualize the shear waves propagate in the thyroid coming from all the larynx area and reverberate at the different interfaces resulting in a complex shear wave field [31].

Some recent studies use similar techniques for clinical applications that exploit Rayleigh waves (surface waves) to highlight skin and lung diseases [32] or induce shear waves at 100, 150 and 200 Hz to quantify the increased intracranial hypertension [33]. These results give us hope for clinical studies of our method that aims to measure viscoelastic parameters by analysis of the space and time spectrum. With the method presented in this paper, we will be able to measure *in vivo* the shear viscosity conjointly with the shear elastic modulus in the 100-300 Hz bandwidth.

REFERENCES

- [1] J. Wuerfel, F. Paul, B. Beierbach, U. Hamhaber, D. Klatt, S. Papazoglou, F. Zipp, P. Martus, J. Braun, and I. Sack, «MR-elastography reveals degradation of tissue integrity in multiple sclerosis.», *NeuroImage***49**(3), 2520-2525 (2010).
- [2] E. Nicolas, S. Callé, S. Nicolle, D. Mitton, and J. P. Remenieras, «Biomechanical characterization of ex vivo human brain using ultrasound shear wave spectroscopy,» *Ultrasonics***84**, 119-125 (2018).
- [3] C. Chartier, Y. Mofid, C. Bastard, V. Miette, A. Maruani, L. Mchet, and F. Ossant, «High-Resolution Elastography for Thin-Layer Mechanical Characterization: Toward Skin Investigation,» *Ultrasound Med. Biol.***43**(3), 670-681 (2016).
- [4] E. Bavu, J. L. Gennisson, M. Couade, J. Bercoff, V. Mallet, M. Fink, A. Badel, A. Vallet-Pichard, B. Nalpas, M. Tanter, and S. PoI, «Noninvasive *in vivo* liver fibrosis evaluation using supersonic shear imaging: a clinical study on 113 hepatitis C virus patients,» *Ultrasound Med. Biol.***37**(9), 1361-1373 (2011).
- [5] L. Sandrin, J. Oudry, C. Bastard, C. Fournier, V. Miette, and S. Mueller, «Non-Invasive Assessment of Liver Fibrosis by Vibration-Controlled Transient Elastography (Fibroscan®),» *Liver Biopsy*, Hirokazu Takahashi, IntechOpen, 293-314 (2011).
- [6] Loree, H., Miette, V., Bastard, C., Sandrin, L., & Cassereau, D. (2018). "Hybrid Elastography: A New Technique for the Assessment of Tissue Stiffness". *2018 IEEE International Ultrasonics Symposium (IUS)*. doi:10.1109/ultsym.2018.8579866
- [7] Deng, Y., Rouze, N. C., Palmeri, M. L., & Nightingale, K. R. (2017). Ultrasonic Shear Wave Elasticity Imaging Sequencing and Data Processing Using a Verasonics Research Scanner. *IEEE Transactions on Ultrasonics, Ferroelectrics, and Frequency Control*, 64(1), 164–176. doi:10.1109/tuffc.2016.2614944
- [8] K. Nightingale, «Acoustic Radiation Force Impulse (ARFI) Imaging: a Review,» *Curr. Med. Imaging Rev.***7**(4), 328-339 (2011).
- [9] J. Bercoff, M. Tanter, and M. Fink, «Supersonic shear imaging: a new technique for soft tissue elasticity mapping,» *IEEE*

- Trans. UltrasonFerroelectr. Freq. Control. **51**(4), 396-409 (2004).
- [10] Thesis A.Zorgani LabTau France (2016) Passive Elastography : Tomography and Mechanical Characterization of Biological Tissue.
- [11] Tzschätzsch et al. Two-Dimensional Time-Harmonic Elastography of the Human Liver and Spleen. *Ultrasound Med Biol.*2016Nov;**42**(11):2562-2571.doi: 10.1016/j.ultrasmedbio.2016.07.004
- [12] Thesis M.Tardieu: "Elastography by magnetic resonance and guided pressure wave". 2014.
- [13] E. Nicolas, S. Callé, and J. P. Remenieras, « Generating Shear Waves in the Human Brain for Ultrasound Elastography: A new Approach, » *Physics Procedia***70**, 1255-1259 (2015).
- [14] S. Catheline, J. L. Gennisson, G. Delon, M. Fink, R. Sinkus, S. Abouelkaram, and J. Culioli, « Measurement of viscoelastic properties of homogeneous soft solid using transient elastography: An inverse problem approach, » *J. Acoust. Soc. Am.***116**(6), 3734-3741 (2004).
- [15] S. Catheline, N. Benez, J. Brum, and C. Negreira, « Time Reversal of Elastic Waves in Soft Solids, » *Phys. Rev. Lett.***100**, 6-15 (2008).
- [16] H. Zhao, P. Song, D. D. Meixner, R. R. Kinnick, M. R. Callstorm, W. Sanchez, M. W. Urban, A. Manduca, J. Greenleaf, L. Fellow, and S. Chen, « External Vibration Multi-directional Ultrasound Shearwave Elastography (EVMUSE): Application in Liver Fibrosis Staging, » *IEEE Trans. Med. Imaging.* **33**(11), 2140–2148 (2014).
- [17] C. J. O'Reilly, « A wave expansion method for acoustic propagation in lined flow ducts, » *Applied Acoustics***90**, 54-63 (2015).
- [18] M. Orescanin, and M. F. Insana, « Shear Modulus Estimation With Vibrating Needle Stimulation, » *IEEE Transactions on Ultrasonics Ferroelectrics and Frequency Control.* **57**(6), 1358-67 (2010).
- [19] F. P. Russell, K. A. Wilkinson, P. H. J. Kelly, and C-K. Skylaris, « Optimised three-dimensional Fourier interpolation: An analysis of techniques and application to a linear-scaling density functional theory code, » *Computer Physics Communications.* **187**, 8-19 (2014).
- [20] M. Couade, M. Pernot, C. Prada, E. Messas, J. Emmerich, P. Bruneval, A. Criton, M. Fink, and M. Tanter, « Quantitative assessment of arterial wall biomechanical properties using shear wave imaging, » *Ultrasound Med. Biol.***36**(10), 662-676 (2010).
- [21] Oudry, Jennifer & Bastard, Cécile & Miette, Veronique & Willinger, R & Sandrin, Laurent. (2009). Copolymer-in-oil Phantom Materials for Elastography. *Ultrasound in medicine & biology.* 35. 1185-97. 10.1016/j.ultrasmedbio.2009.01.012.
- [22] C. Kasai, K. Namekawa, A. Koyano, and R. Omoto, « Real-Time Two-Dimensional Blood Flow Imaging Using an Autocorrelation Technique, » *IEEE Transactions on Sonics and Ultrasonics.* **32**(3) 458- 464 (1985).
- [23] A. P. Hoeks, P. J. Brands, T. G. Arts, and R. S. Reneman, « Subsample volume processing of doppler 590 ultrasound signals, » *Ultrasound Med. Biol.* **20**(9), 953-965 (1994).
- [24] R. Rouffaud, S. Beuve, L. Kritly, and J. P. Remenieras, « In Vivo Contractile Properties Measurement of the Biceps Brachii Muscle Using High Frame Rate Plane Waves And k-Space Transverse Oscillation, » *in Proceedings of IEEE Ultrasonics Symposium, Washington, United States of America* (2017), pp. 188-189.
- [25] N. Benez, S. Catheline, J. Brum, T. Gallot, and C. A. Negreira, « 1-D Elasticity Assessment in Soft Solids from Shear Wave Correlation: The Time-Reversal Approach, » *IEEE Transactions on Ultrasonics, Ferroelectrics, and Frequency Control***56**(11), 2400-2410 (2011).
- [26] A. Derode, E. Larose, M. Campillo, and M. Fink, « How to estimate the Green's function of a heterogeneous medium between two passive sensors? Application to acoustic waves, » *Applied Physics Letters***83**(15), 3054-3056 (2003).
- [27] M. W. Urban, S. Chen, and M. A. Fatemi, « A Review of Shearwave Dispersion Ultrasound Vibrometry (SDUV) and its Applications, » *Curr. Med. Imaging Rev.* **8**(1), 27–36 (2012).
- [28] [1] Kijanka, P., Qiang, B., Song, P., Amador Carrascal, C., Chen, S., & Urban, M. W. (2018). Robust Phase Velocity Dispersion Estimation of Viscoelastic Materials Used for Medical Applications Based on the Multiple Signal Classification Method. *IEEE Transactions on Ultrasonics, Ferroelectrics, and Frequency Control*, 65(3), 423–439. doi:10.1109/tuffc.2018.2792324
- [29] Sack, I., Jöhrens, K., Würfel, J., & Braun, J. (2013). Structure-sensitive elastography: on the viscoelastic powerlaw behavior of in vivo human tissue in health and disease. *Soft Matter*, 9(24), 5672-5680.
- [30] Lee, W. N., Chang, E. J. H., Guo, Y., & Wang, Y. (2018). Experimental investigation of guided wave imaging in thin soft media under various coupling conditions. *Ultrasound in medicine & biology*, 44(12), 2821-2837.
- [31] S. Beuve, E. Khoury, S. Callé, and J. P. Remenieras, « Elastography of the thyroid by tracking shear waves generated by vocal cord vibrations, » *in Proceedings of IEEE Ultrasonics Symposium, Kobe, Japan* (2018), pp. 208.
- [32] X Zhang, B Zhou, S Kalra, B Bartholmai, J Greenleaf, T Osborn. An Ultrasound Surface Wave Technique for Assessing Skin and Lung Diseases. *Ultrasound in Medicine & Biology.* 44. 10.1016/j.ultrasmedbio.2017.10.010.
- [33] B Zhou, J Chen, A Kazemi, A Sit, X Zhang. (2019). An Ultrasound Vibro-Elastography Technique for Assessing Papilledema. *Ultrasound in Medicine & Biology.* 45. 10.1016/j.ultrasmedbio.2019.04.029.